Microplane-Triad Model for Elastic and Fracturing Behavior of Woven Composites

Kedar Kirane
Civil and Environmental Engineering,
Northwestern University,
Evanston, IL 60201
e-mail: kedarkirane2011@u.northwestern.edu

Marco Salviato
Civil and Environmental Engineering,
Northwestern University,
Evanston, IL 60201
e-mail: marco.salviato@northwestern.edu

Zdeněk P. Bažant[1]
Distinguished McCormick Institute Professor and
W.P. Murphy Professor
ASME Honorary Member
Civil and Environmental Engineering and
Materials Science,
Northwestern University,
Evanston, IL 60201
e-mail: z-bazant@northwestern.edu

A multiscale model based on the framework of microplane theory is developed to predict the elastic and fracturing behavior of woven composites from the mesoscale properties of the constituents and the weave architecture. The effective yarn properties are obtained by means of a simplified mesomechanical model of the yarn, based on a mixed series and parallel coupling of the fibers and of the polymer within the yarns. As a novel concept, each of the several inclined or aligned segments of an undulating fill and warp yarn is represented by a triad of orthogonal microplanes, one of which is normal to the yarn segment while another is normal to the plane of the laminate. The constitutive law is defined in terms of the microplane stress and strain vectors. The elastic and inelastic constitutive behavior is defined using the microplane strain vectors which are the projections of the continuum strain tensor. Analogous to the principle of virtual work used in previous microplane models, a strain energy density equivalence principle is employed here to obtain the continuum level elastic and inelastic stiffness tensors, which in turn yield the continuum level stress tensor. The use of strain vectors rather than tensors makes the modeling conceptually clearer as it allows capturing the orientation of fiber failures, yarn cracking, matrix microcracking, and interface slip. Application of the new microplane-triad model for a twill woven composite shows that it can realistically predict all the orthotropic elastic constants and the strength limits for various layups. In contrast with the previous (nonmicroplane) models, the formulation can capture the size effect of quasi-brittle fracture with a finite fracture process zone (FPZ). Explicit finite-element analysis gives a realistic picture of progressive axial crushing of a composite tubular crush can initiated by a divergent plug. The formulation is applicable to widely different weaves, including plain, twill, and satin weaves, and is easily extensible to more complex architectures such as hybrid weaves as well as two- and three-dimensional braids.
[DOI: 10.1115/1.4032275]

1 Introduction

Composite materials reinforced with woven fabric preforms have become an attractive high-performance alternative to metals in many engineering applications from land, marine, and air transportation and wind and tidal energy production, to blast protection of civil infrastructures and automotive crashworthiness. This is owed to their outstanding specific stiffness, strength, and energy absorption capability, combined with their unique adaptability to complex shapes [1,2].

To take advantage of the excellent characteristics of these composites, their constitutive model must capture damage and fracture. This is a challenging task, since it requires the main mechanisms of damage in the mesostructure to be linked to the macroscopic fracture initiation and propagation. Although textile composites have been studied extensively, the main focus has been on linear elastic behavior, see Refs. [3–15].

The first model to predict the main mechanical properties of woven and braided composites, including damage and failure, was proposed by Naik [16]. His model is based on a micromechanical analysis that discretely models the yarn architecture within a repeated representative unit cell (RUC). An isostrain condition within the RUC is then assumed to get the homogenized mechanical properties after accounting for the effects of nonlinear shear response and local damage accumulation. However, the predictions were accurate only for axial response under uniaxial loading aligned with the yarn. They were not for the highly nonlinear off-axis response.

Based on the so-called classical laminate theory, a similar formulation for predicting the elastic moduli and strengths of hybrid and nonhybrid woven composites was presented by Scida et al. [17]. Failure of the constituents was modeled through empirical strength criteria. In particular, the von Mises criterion was applied to determine the failure of the matrix whereas failure of the fill and warp yarns was described by the Tsai-Wu criterion [18]. This model neglected the progressive damage in the mesostructure. It could not predict the highly nonlinear off-axis behavior under yarn-aligned uniaxial loading, which is affected by subcritical microcracking of the matrix, endemic for textile composites (see, e.g., Ref. [19]). Its modeling is the key to predict the energy absorption capability. Similar results were obtained in Refs. [20,21].

An attempt for accurate modeling of progressive damage in the mesostructure, including fiber failure and matrix microcracking, was made by Prodromou et al. [22]. The authors proposed a numerical model of the RUC based on the method of cells, by which they accounted for the geometry of the mesostructure while describing the degradation and failure of the constituents in a conventional way. The use of cells allowed predicting the elastic properties more accurately than analytical approaches and improved prediction of the off-axis behavior under yarn-aligned uniaxial loads.

In general, finite-element mesoscale models of the RUC were found to be more effective than analytical models in representing the effects of yarn undulation and microcracking damage [23]. However, this was achieved at the expense of simplicity and computational efficiency. The numerical analysis of each RUC involves many degrees-of-freedom. This hinders applications to structures comprising many RUCs.

---

[1]Corresponding author.

Here, we strive for a model that is both accurate and computationally effective. Based on experience with other quasi-brittle materials, this goal can be attained by the microplane approach, which has already been used by Caner et al. [24] for braided composite. Their model yielded excellent estimates of the axial stiffness under axial loading and led to acceptable though less than perfect agreement with the tests of fracture energy and size effect. However, it could not provide accurate estimates of the orthotropic elastic constants for shear and for axial–lateral coupling. This drawback is overcome here by introducing the new concept of microplane triads.

2 Microplane Model for Elastic Behavior

The microplane theory was originally developed to describe the softening damage of heterogeneous but statistically isotropic materials, such as concrete and rocks [25,26]. A key feature of the microplane model is that the constitutive law is formulated in terms of the stress and strain vectors acting on a generic plane of any orientation within the material mesostructure, called the *microplane*. The microplane strain vectors are the projections of the macroscopic (continuum) strain tensor, whereas the macroscopic stress tensor is related variationally to the microplane stress vectors via the principle of virtual work. The adoption of vectors rather than tensors makes the approach conceptually clearer, while the introduction of microplanes allows embedding the effect of the mesostructure into the formulation [27–29].

In the past, several approaches to apply the microplane concept to anisotropic materials have been explored [24,30–32]. However, the role played by the mesoscale constituents (e.g., fibers and matrix) in determining the overall mechanical behavior was not clarified. In the present formulation, a multiscale microplane theory is proposed to predict the anisotropic elastic and fracturing behavior of woven composites based on the mechanical properties of the constituents and the weave architecture. This is achieved by using microplanes with a preferential orientation, a concept that is equivalent to assigning zero stiffness to microplanes of all other orientations, thus automatically introducing anisotropy. This concept was already introduced earlier and was shown to predict well the axial moduli of braided composites [24], though not the shear moduli and Poisson effects. Here, the key idea is to introduce the concept of microplane triads, which makes it possible to predict the full range of orthotropic elastic constants, multiaxial strength limits, and fracturing behavior for various woven composites.

2.1 Stiffness Tensor for One RUC.
The microplane model characterizes at one continuum point the average behavior of one RUC, defined as the smallest cell that gets periodically repeated within the woven composite. For one RUC, we introduce a local coordinate system in which 1 and 2 represent the fill and warp yarn directions, respectively. Then, the local direction 3 is the out-of-plane normal, see Fig. 1(a) for a twill 2×2 woven composite.

Each RUC is imagined to consist of three parallel plates, namely (1) the fill yarn plate, (2) the warp yarn plate, and (3) the pure matrix (or polymer) plate, as shown in Fig. 1(b). These are assumed to act in parallel coupling, i.e., each plate is assumed to be under the same state of uniform strain [11,24,33]. The elastic stiffness tensor of the RUC is then expressed as

$$\mathbf{K}^{\mathrm{RUC}} = \frac{V_{\mathrm{y}}}{2} \mathbf{K}^{\mathrm{FY}} + \frac{V_{\mathrm{y}}}{2} \mathbf{K}^{\mathrm{WY}} + (1 - V_{\mathrm{y}}) \mathbf{K}^{\mathrm{M}} \qquad (1)$$

where $\mathbf{K}^{\mathrm{RUC}}$, $\mathbf{K}^{\mathrm{FY}}$, $\mathbf{K}^{\mathrm{WY}}$, and $\mathbf{K}^{\mathrm{M}}$ represent the fourth-order stiffness tensors of the RUC, fill yarn plate, warp yarn plate, and pure matrix plate, respectively, and V_{y} is the volume fraction of the yarn (or the tow) within one RUC. Note that this is the volume fraction not of the pure fiber (V_{f}), but of the *yarn* within the RUC. The yarn itself includes some matrix material (or polymer) that lies between the individual fiber strands. Equation (1) relates the elastic stiffness tensor of one RUC to the stiffness tensors of its
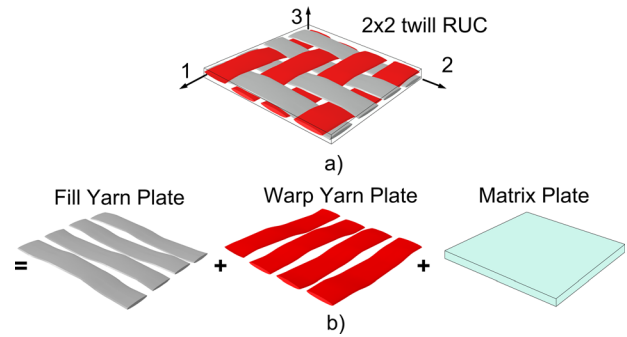
Fig. 1 Schematic representation of (*a*) the RUC of a 2×2 twill composite and its local coordinate system and (*b*) decomposition of the RUC into matrix, fill and warp yarn plates assumed to be in parallel coupling

constituents at the lower scale, which are derived in Secs. 2.2 and 2.3.

2.2 Stiffness Tensor for the Matrix Plate.
Since the matrix is homogenous and isotropic, its fourth-order elastic stiffness tensor is given by

$$K_{ijkl}^{\mathrm{M}} = \frac{E^m}{3(1 - 2\nu^m)} \delta_{ij}\delta_{kl} + \frac{E^m}{2(1 + \nu^m)} \left(\delta_{ik}\delta_{jl} + \delta_{il}\delta_{jk} - \frac{2}{3}\delta_{ij}\delta_{kl} \right) \qquad (2)$$

Here, subscripts i, j, k, and l go from 1 to 3, and δ_{ij} is the Kronecker delta or the second-order identity tensor, such that $\delta_{ij} = 1$ when $i = j$ and $\delta_{ij} = 0$ when $i \neq j$. E^m and ν^m denote the Young's modulus and Poisson ratio of the matrix. There is no need for microplane modeling of the matrix plate.

2.3 Stiffness Tensor for the Yarn Plates.
The stiffness tensor of the yarn plates (fill and warp) is derived by applying the microplane theory. To describe the yarn stiffness, we introduce microplane triads along the yarn. Each triad consists of three mutually orthogonal microplanes and is oriented such that one of the microplane normals, **n**, be always tangential to the yarn curve and the other microplane has a normal vector **m** parallel to the yarn plate.

Then, the stiffness tensors of the yarn plates $\mathbf{K}^{\mathrm{FY}}$ and $\mathbf{K}^{\mathrm{WY}}$ are obtained by imposing strain energy density equivalence. It is stipulated that the strain energy density at yarn plate level be equal to the volume averaged strain energy density at microplane level. So if T^{YP} and T^{μ} represent the strain energy densities at the yarn plate level and microplane level, respectively, we have

$$T^{\mathrm{YP}} = \frac{1}{AL} \int_V T^{\mu} dV = \frac{1}{L} \int_L T^{\mu} dL \qquad (3)$$

where A is the yarn plate cross-sectional area, L is the curvilinear length of the yarn, V is the yarn plate volume $= AL$, and $dV = AdL$.

The above integral would be unbiased and exact if there were an infinite number of microplane triads along the yarn. Here, a discrete approximation of this integral is introduced. This is achieved by the discretization of the yarn undulation path into segments. As shown in Fig. 2(a), at least six yarn segments are required to discretize the undulating path of each yarn within the chosen RUC. Note that the volume associated with the strain energy density of each segment is now finite and equal to $A^{\mu}L^{\mu}$, where A^{μ} is the cross-sectional area of that segment, and L^{μ} its curvilinear length. Note that here A^{μ} is considered to be constant, although a variable A^{μ} could easily be accounted for.

One microplane triad is introduced for each yarn segment. It is oriented such that the normal **n** of one of the three microplanes be
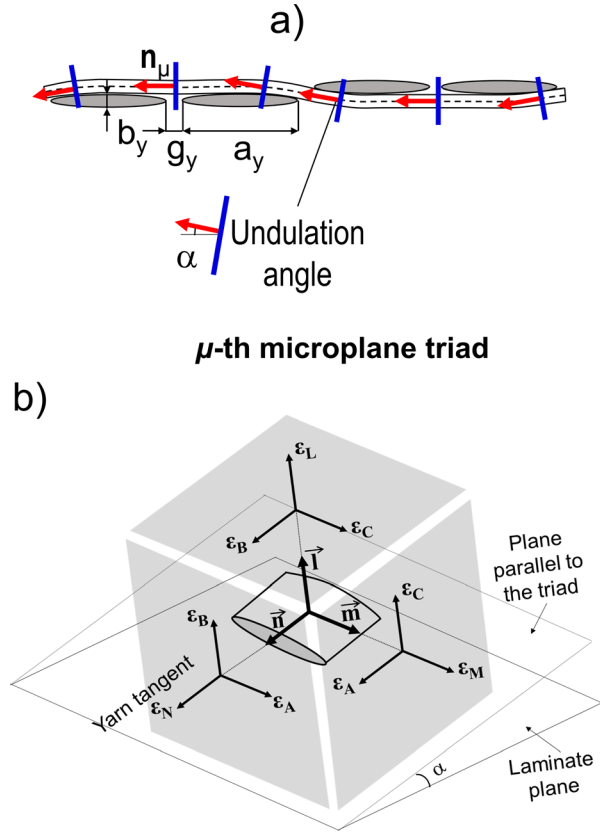
Fig. 2 (*a*) **Example of discretization of the yarn into microplanes for a twill** 2×2 **and** (*b*) **projection of the strain tensor into the** μ **th microplane triad**

parallel to the yarn curve at the center of the segment. From the angle of that normal with respect to the yarn plate, denoted α (Fig. 2(*a*)), the direction cosines of the normals of all the microplanes in the triad follow. For each triad, vectors **m** and **l** are normal to the local yarn direction. The vectors **n**, **m**, and **l** form a right-handed triad of vectors.

Angle α is related to the aspect ratio of the elliptical yarn cross section and is given by

$$\alpha = \tan^{-1}[b_y/(a_y + g_y)] \tag{4}$$

where a_y is the major axis of the elliptical yarn cross section, b_y its minor axis (equal to the yarn thickness), and g_y is the average gap between the yarns. Microplanes triads are introduced in both the fill and warp directions. Due to assumed symmetry, the α values for both the fill and warp yarns are the same. Then, the microplanes for the warp yarn are nothing but the fill yarn microplanes rotated by 90 deg about the RUC coordinate vector 3. Note that a different undulation angle for the fill and warp yarns could easily be used when dealing with another composite.

Integral (3) can be discretely approximated as a weighted average of the strain energy of all the six microplane triads

$$T^{\mathrm{YP}} = \sum_{\mu=1}^{6} w^\mu T^\mu \tag{5}$$

Here, μ is the number of the microplane triads, and w^μ is the weight of triad μ, given by

$$w^\mu \approx L^\mu/L \tag{6}$$

where L^μ is the length of the yarn segment corresponding to the microplane triad μ. Thus, the microplane stiffness is weighted in

proportion to the fraction of yarn length occupied by that orientation. For example, for a plain weave, the weights of all microplane triads would be equal and equal to 1/6, but for a satin weave they would be unequal [33]. The weights are normalized by the partition of unity, so $\sum_{\mu=1}^{6} w^\mu = 1$. Note that, in contrast to the standard isostrain assumption, the present microplane model with the aforementioned weighted sum leads to microplane strain vectors differing in magnitude from the strain tensor projection.

Once the total strain energy density is computed, the stiffness tensor of the yarn plate is defined as

$$K_{ijkl}^{\mathrm{YP}} = \frac{\partial^2 T^{\mathrm{YP}}}{\partial \varepsilon_{ij} \partial \varepsilon_{kl}} \tag{7}$$

This approach is a conceptual parallel to the principle of virtual work, used in the conventional microplane model for statistically isotropic particulate composites (e.g., concrete) to relate the macro- and microplane stresses.

2.3.1 Strain Energy at Microplane Level. The strain energy for each microplane triad is obtained by noting that each segment of the yarn, by itself, represents a unidirectional, transversely isotropic composite consisting of pure fibers and interfiber matrix. The macroscopic (continuum) strain tensor ε_{ij} is projected on each microplane of each triad (Fig. 2(*b*)). This projection gives the normal microplane strain

$$\varepsilon_N = \varepsilon_{ij} n_i n_j \tag{8}$$

in the direction of the yarn segment. The transverse normal strains in the triad are given by

$$\varepsilon_M = \varepsilon_{ij} m_i m_j, \quad \varepsilon_L = \varepsilon_{ij} l_i l_j \tag{9}$$

The shear strain vectors for each microplane in the triad are simply given by

$$\varepsilon_A = \frac{1}{2} \varepsilon_{ij}(n_i m_j + m_i n_j), \quad \varepsilon_B = \frac{1}{2} \varepsilon_{ij}(n_i l_j + l_i n_j),$$
$$\varepsilon_C = \frac{1}{2} \varepsilon_{ij}(m_i l_j + l_i m_j) \tag{10}$$

These strain vectors are now used to derive the strain energy density for the microplane triad, as one unit. Note that while, in previous formulations of the microplane model, ε_M and ε_L denoted the shear strain vectors, here they denote the transverse normal strain vectors and the shear strain vectors are denoted by ε_A, ε_B, and ε_C.

This change in notation is necessary because of using microplane triads instead of individual microplanes. Herein lays the essential difference of the present microplane model from the conventional microplane models for statistically isotropic materials. In the conventional models, the orientations of microplane normals sample the optimal Gaussian integration points for the evaluation of an integral over all the spatial directions (i.e., over the surface of a hemisphere). Each of these microplanes is characterized by the normal strain and two shear strains. Refining the Gaussian integration scheme converges to the integral, which guarantees tensorial invariance. The normal and shear moduli on the microplanes control the values of the macroscopic shear moduli and Poisson ratio.

For an orthotropic material, the invariance restrictions are different and more complex. The present approach with microplane triads representing the well defined microstructure avoids dealing with these restrictions and produces an orthotropic material stiffness tensor directly. It is important that each microplane triad is characterized by three normal strains, one for each microplane in the triad, and three shear strain components (note that each shear strain is common to two microplanes in the triad). Note that in the plane normal to the yarn segment, the response of the yarn segment is isotropic.

A properly representative choice of microplanes is, of course, important. This is exemplified by comparison with the preceding model [24] that featured the microplanes normal to yarn segments but missed the microplanes parallel to the yarn. That model, applied to a braided composite, could not capture the Poisson and shear effects accurately.

Another difference from the previous formulation in Ref. [24] is the use of the strain energy approach to derive the stiffness tensor for each microplane triad. Although the equilibrium conditions obtained by the derivatives of strain energy are equivalent to those expressed by the principle of virtual work in previous microplane models, the present energy approach is convenient for ensuring the inclusion of all the deformation modes, including the volumetric and deviatoric ones, and for automatically capturing the Poisson and shear effects.

The strain energy density T^μ for one yarn segment represented by a microplane triad is written as [33,34]

$$
\begin{aligned}
T^\mu = {} & A_1 \varepsilon_N^2 + A_2 \varepsilon_M^2 + A_3 \varepsilon_L^2 \\
& + \frac{A_4}{2}(\varepsilon_N \varepsilon_M + \varepsilon_M \varepsilon_N) + \frac{A_5}{2}(\varepsilon_N \varepsilon_L + \varepsilon_L \varepsilon_N) + \frac{A_6}{2}(\varepsilon_M \varepsilon_L + \varepsilon_L \varepsilon_M) \\
& + A_7 \varepsilon_A^2 + A_8 \varepsilon_B^2 + A_9 \varepsilon_C^2
\end{aligned}
\tag{11}
$$

where $A_1, A_2 \ldots A_9$ are the functions of the elastic constants of the yarn and will be described later. Substituting Eq. (8) in the first term of the foregoing expression, one gets

$$
T_1 = A_1 \varepsilon_N^2 = A_1 (\varepsilon_{ij} n_i n_j)^2 = A_1 (\varepsilon_{ij} n_i n_j)(\varepsilon_{kl} n_k n_l)
\tag{12}
$$

(index repetition implies summation). Similarly, the second and third term become

$$
T_2 = A_2 (\varepsilon_{ij} m_i m_j)(\varepsilon_{kl} m_k m_l); \quad T_3 = A_3 (\varepsilon_{ij} l_i l_j)(\varepsilon_{kl} l_k l_l)
\tag{13}
$$

Terms 4–6 involve cross terms and become

$$
\begin{aligned}
T_4 &= \frac{A_4}{2}\left[(\varepsilon_{ij} n_i n_j)(\varepsilon_{kl} m_k m_l) + (\varepsilon_{ij} m_i m_j)(\varepsilon_{kl} n_k n_l)\right] \\
T_5 &= \frac{A_5}{2}\left[(\varepsilon_{ij} n_i n_j)(\varepsilon_{kl} l_k l_l) + (\varepsilon_{ij} l_i l_j)(\varepsilon_{kl} n_k n_l)\right] \\
T_6 &= \frac{A_6}{2}\left[(\varepsilon_{ij} m_i m_j)(\varepsilon_{kl} l_k l_l) + (\varepsilon_{ij} l_i l_j)(\varepsilon_{kl} m_k m_l)\right]
\end{aligned}
\tag{14}
$$

Likewise, terms 7–9 are given by

$$
\begin{aligned}
T_7 &= A_7 (\varepsilon_{ij} a_i a_j)(\varepsilon_{kl} a_k a_l) \\
T_8 &= A_8 (\varepsilon_{ij} b_i b_j)(\varepsilon_{kl} b_k b_l) \\
T_9 &= A_9 (\varepsilon_{ij} c_i c_j)(\varepsilon_{kl} c_k c_l)
\end{aligned}
\tag{15}
$$

where $a_i a_j = 1/2(n_i m_j + m_i n_j)$, $b_i b_j = 1/2(n_i l_j + l_i n_j)$ and $c_i c_j = 1/2(m_i l_j + l_i m_j)$. Now, substitution of the foregoing expression into Eqs. (5) and (7) yields the expression for the stiffness tensor of the yarn plate

$$
\begin{aligned}
K_{ijkl}^{\mathrm{YP}} = 2 \sum_{\mu=1}^{6} w^\mu \Big[& A_1 N_{ij} N_{kl} + A_2 M_{ij} M_{kl} + A_3 L_{ij} L_{kl} + \frac{A_4}{2}(N_{ij} M_{kl} + N_{kl} M_{ij}) \\
& + \frac{A_5}{2}(N_{ij} L_{kl} + N_{kl} L_{ij}) + \frac{A_6}{2}(M_{ij} L_{kl} + M_{kl} L_{ij}) + A_7 \Phi_{ij} \Phi_{kl} \\
& + A_8 \Upsilon_{ij} \Upsilon_{kl} + A_9 \Psi_{ij} \Psi_{kl} \Big]^\mu
\end{aligned}
\tag{16}
$$

where $N_{ij} = n_i n_j$, $M_{ij} = m_i m_j$, $L_{ij} = l_i l_j$, $\Phi_{ij} = a_i a_j$, $\Upsilon_{ij} = b_i b_j$, and $\Psi_{ij} = c_i c_j$. A more detailed description of the foregoing equations and the role played by each term of Eq. (16) can be found in Ref. [33].

It should be noted that, thanks to the foregoing microplane formulation, the effect of the mesostructure is automatically embedded. On the other hand, the important role played by each constituent is introduced through the terms A_i ($i = 1 \ldots 9$), which are functions of the elastic properties of the fibers and the matrix in the yarn. Their derivation is presented in Sec. 2.3.2.

2.3.2 Effective Elastic Properties of the Yarn. To explain the parameters $A_1, A_2 \ldots A_9$ that populate the microplane stiffness tensor, the effective properties of the yarn are calculated using a mesomechanics approach. Let the superscript Y denote the yarn properties, m the matrix properties, and f the pure fiber properties. In this context, the term "matrix" now implies the matrix in between the pure fibers within one yarn.

Various mesoscale simulations suggest that the matrix between the fibers within a yarn works in transferring the loads in the lateral direction and stiffens the axial response. This may be approximated by considering a parallel coupling of the matrix with pure fibers in the axial direction, but a series coupling in the transverse direction. Accordingly, we have, for the yarn

$$
E_{1'}^{\mathrm{Y}} = V_f^{\mathrm{Y}} E_{1'}^{\mathrm{f}} + (1 - V_f^{\mathrm{Y}}) E^m
\tag{17}
$$

where $E_{1'}^{\mathrm{Y}}$ is the axial modulus of the yarn, $E_{1'}^{\mathrm{f}}$ is the axial modulus of the fiber, E^m is the modulus of the matrix, and V_f^{Y} is the fiber volume fraction *within one yarn*. For the transverse directions, we assume a series coupling. So

$$
E_{2'}^{\mathrm{Y}} = E_{3'}^{\mathrm{Y}} = \left(\frac{V_f^{\mathrm{Y}}}{E_{2'}^{\mathrm{f}}} + \frac{1 - V_f^{\mathrm{Y}}}{E^m} \right)^{-1}
\tag{18}
$$

where $E_{2'}^{\mathrm{Y}} = E_{3'}^{\mathrm{Y}}$ and $E_{2'}^{\mathrm{f}} = E_{3'}^{\mathrm{f}}$ are the transverse moduli of the yarn and the fibers, respectively. Here, the suffix $1'$ denotes the axial direction of the yarn, while the plane $2' - 3'$ is the cross section of the yarn as shown in Fig. 3. The "prime" is introduced to distinguish these directions from those of the RUC coordinate system (where direction 1 is the fill yarn, and direction 2 is the warp).

For the in-plane shear response, it is common to assume a self-consistent scheme of coupling [35], which provides better estimates compared to a pure series coupling. Accordingly

$$
G_{1'2'}^{\mathrm{Y}} = G_{1'3'}^{\mathrm{Y}} = G^m \frac{(G_{1'2'}^{\mathrm{f}} + G^m) + V_f^{\mathrm{Y}}(G_{1'2'}^{\mathrm{f}} - G^m)}{(G_{1'2'}^{\mathrm{f}} + G^m) - V_f^{\mathrm{Y}}(G_{1'2'}^{\mathrm{f}} - G^m)}
\tag{19}
$$

For the out-of-plane shear elastic modulus, a series, rather than parallel, coupling is appropriate. So

$$
G_{2'3'}^{\mathrm{Y}} = \left(\frac{V_f^{\mathrm{Y}}}{G_{2'3'}^{\mathrm{f}}} + \frac{1 - V_f^{\mathrm{Y}}}{G^m} \right)^{-1}
\tag{20}
$$

where $G_{1'2'}^{\mathrm{Y}}, G_{1'3'}^{\mathrm{Y}}$, and $G_{2'3'}^{\mathrm{Y}}$ represent the shear moduli of the yarn, $G_{1'2'}^{\mathrm{f}}, G_{1'3'}^{\mathrm{f}}$, and $G_{2'3'}^{\mathrm{f}}$ are the shear moduli of the fiber, and $G^m = E^m/2(1 + \nu^m)$ is the shear modulus of the matrix.
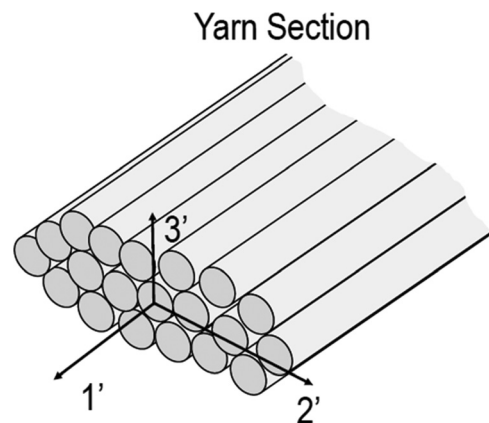
Yarn Section

Fig. 3 Local coordinate system assigned to each yarn section

For all the Poisson ratios of the yarn, the following relations are considered:

$$\nu_{1'2'}^{Y} = V_f^{Y}\nu_{1'2'}^{f} + (1 - V_f^{Y})\nu^{m}; \quad \nu_{1'3'}^{Y} = V_f^{Y}\nu_{1'3'}^{f} + (1 - V_f^{Y})\nu^{m};$$
$$\nu_{2'3'}^{Y} = V_f^{Y}\nu_{2'3'}^{f} + (1 - V_f^{Y})\nu^{m} \tag{21}$$

These effective properties are used to obtain the fourth-order elasticity tensor of the yarn. Note that $1' - 2'$, $1' - 3'$, and $2' - 3'$ are the three planes of material symmetry, the elastic tensor of the yarn, denoted as C_{pq} ($p, q = 1$–6), can be written as follows:

$$
\begin{bmatrix} \sigma_{1'} \\ \sigma_{2'} \\ \sigma_{3'} \\ \tau_{1'2'} \\ \tau_{2'3'} \\ \tau_{1'3'} \end{bmatrix}
=
\begin{bmatrix}
C_{1'1'} & C_{1'2'} & C_{1'3'} & 0 & 0 & 0 \\
C_{1'2'} & C_{2'2'} & C_{2'3'} & 0 & 0 & 0 \\
C_{1'3'} & C_{2'3'} & C_{3'3'} & 0 & 0 & 0 \\
0 & 0 & 0 & C_{4'4'} & 0 & 0 \\
0 & 0 & 0 & 0 & C_{5'5'} & 0 \\
0 & 0 & 0 & 0 & 0 & C_{6'6'}
\end{bmatrix}
\begin{bmatrix} \varepsilon_{1'} \\ \varepsilon_{2'} \\ \varepsilon_{3'} \\ \gamma_{1'2'} \\ \gamma_{2'3'} \\ \gamma_{1'3'} \end{bmatrix}
\tag{22}
$$

The various C_{pq} are obtained from the effective yarn properties as [35]

$$C_{1'1'}^{Y} = \frac{1 - \nu_{2'3'}^{Y}\nu_{3'2'}^{Y}}{E_{2'}^{Y}E_{3'}^{Y}\Delta}; \quad C_{2'2'}^{Y} = \frac{1 - \nu_{1'3'}^{Y}\nu_{3'1'}^{Y}}{E_{1'}^{Y}E_{3'}^{Y}\Delta}; \quad C_{3'3'}^{Y} = \frac{1 - \nu_{1'2'}^{Y}\nu_{2'1'}^{Y}}{E_{1'}^{Y}E_{2'}^{Y}\Delta} \tag{23}$$

and

$$C_{1'2'}^{Y} = \frac{\nu_{1'2'}^{Y} + \nu_{1'3'}^{Y}\nu_{3'2'}^{Y}}{E_{1'}^{Y}E_{2'}^{Y}\Delta}; \quad C_{1'3'}^{Y} = \frac{\nu_{2'3'}^{Y} + \nu_{2'1'}^{Y}\nu_{1'3'}^{Y}}{E_{1'}^{Y}E_{3'}^{Y}\Delta};$$
$$C_{2'3'}^{Y} = \frac{\nu_{3'1'}^{Y} + \nu_{2'1'}^{Y}\nu_{3'2'}^{Y}}{E_{2'}^{Y}E_{3'}^{Y}\Delta} \tag{24}$$

and

$$C_{4'4'}^{Y} = G_{1'2'}^{Y}; \quad C_{5'5'}^{Y} = G_{2'3'}^{Y}; \quad C_{6'6'}^{Y} = G_{1'3'}^{Y} \tag{25}$$

$$\Delta = \frac{1}{E_{1'}^{Y}E_{2'}^{Y}E_{3'}^{Y}}
\begin{vmatrix}
1 & -\nu_{2'1'}^{Y} & -\nu_{3'1'}^{Y} \\
-\nu_{1'2'}^{Y} & 1 & -\nu_{3'2'}^{Y} \\
-\nu_{1'3'}^{Y} & -\nu_{2'3'}^{Y} & 1
\end{vmatrix}
\tag{26}$$

Then, using the various C_{pq}, one can calculate parameters $A_1, A_2, ...A_9$ from the relations given in Refs. [33,34]. Dropping, for brevity, superscript Y, one may express them as

$$A_1 = \frac{1}{2D}\left[(C_{1'1'} + C_{1'2'} + C_{1'3'})^2 + C_{1'1'}(C_{2'2'} + 2C_{2'3'} + C_{3'3'}) \right.$$
$$\left. - (C_{1'2'} + C_{1'3'})^2\right] \tag{27}$$

$$A_2 = \frac{1}{2D}\left[(C_{1'2'} + C_{2'2'} + C_{2'3'})^2 + C_{2'2'}(C_{1'1'} + 2C_{1'3'} + C_{3'3'}) \right.$$
$$\left. - (C_{1'2'} + C_{2'3'})^2\right] \tag{28}$$

$$A_3 = \frac{1}{2D}\left[(C_{1'3'} + C_{2'3'} + C_{3'3'})^2 + C_{3'3'}(C_{1'1'} + 2C_{1'2'} + C_{2'2'}) \right.$$
$$\left. - (C_{1'3'} + C_{2'3'})^2\right] \tag{29}$$

$$A_4 = \frac{1}{2D}\left[2(C_{1'1'} + C_{1'2'} + C_{1'3'})(C_{1'2'} + C_{2'2'} + C_{2'3'}) \right.$$
$$+ 2(C_{1'2'}^2 - (C_{1'1'} + C_{1'3'})(C_{2'2'} + C_{2'3'})$$
$$\left. + C_{1'2'}(C_{1'3'} + C_{2'3'} + C_{3'3'}))\right] \tag{30}$$

$$A_5 = \frac{1}{2D}\left[2(C_{1'2'} + C_{2'2'} + C_{2'3'})(C_{1'3'} + C_{2'3'} + C_{3'3'}) \right.$$
$$+ 2(C_{2'3'}(C_{1'1'} + C_{2'3'}) + C_{1'3'}(-C_{2'2'} + C_{2'3'})$$
$$- C_{2'2'}C_{3'3'} - C_{1'2'}(C_{1'3'} - C_{2'3'} + C_{3'3'}))] \tag{31}$$

$$A_6 = \frac{1}{2D}\left[2(C_{1'3'} + C_{2'3'} + C_{3'3'})(C_{1'1'} + C_{1'2'} + C_{1'3'}) \right.$$
$$+ 2(C_{1'3'}(C_{1'3'} + C_{2'2'} + C_{2'3'}) - C_{1'1'}(C_{2'3'} + C_{3'3'})$$
$$- C_{1'2'}(-C_{1'3'} + C_{2'3'} + C_{3'3'}))] \tag{32}$$

$$A_7 = C_{4'4'}/2 \quad A_8 = C_{5'5'}/2 \quad A_9 = C_{6'6'}/2 \tag{33}$$

where

$$D = C_{1'1'} + C_{2'2'} + C_{3'3'} + 2C_{1'2'} + 2C_{1'3'} + 2C_{2'3'} \tag{34}$$

Thus, using the computed values of $A_1, A_2, ...A_9$ and Eq. (16), one can obtain the stiffness tensor for the yarn plates.

2.4 Summary of the Calculation of the Orthotropic Stiffness Constants. The proposed formulation computes the stiffness tensor of the RUC starting from the individual mesoscale constituents and then systematically proceeds to the macroscale [Matrix + Fibers → Yarn → Microplane → Yarn plate → RUC]. This lends the model a hierarchical multiscale character. To summarize, the procedure consists of five steps:

(1) Obtain the effective properties of the yarn from the properties of the matrix and the fiber, given by Eqs. (17)–(21);
(2) Calculate the components of the elasticity tensor of the yarn, by considering it to be a unidirectional composite, given by Eqs. (23)–(26);
(3) Calculate the prefactors $A_1, A_2, ...$, given by Eqs. (27)–(34);
(4) Calculate the stiffness tensor for the fill and warp yarn plates from the prefactors and the microplane orientations; and
(5) Calculate the stiffness tensor of the RUC using Eq. (1).

3 Microplane Model for Fracturing Behavior

Unidirectional and textile composites are inherently quasi-brittle owing to their heterogeneous microstructure [24,31,36]. In quasi-brittle fracture, the crack tip is surrounded by a nonlinear zone most of which represents an FPZ undergoing softening damage. The quasi-brittleness is due to the fact that the FPZ is not negligible compared to the cross section dimension of the structure. The stress along the FPZ is nonuniform and decreases with the crack opening gradually. In composites, this behavior occurs due to finiteness of the RUC, distributed cracking in the FPZ, crack bridging by fibers, and frictional pullout of inhomogeneities. The relatively large size of the FPZ greatly enhances the energy dissipation capability and endows the material with a certain measure of ductility when the structure is small. An important general attribute of quasi-brittleness is the size effect, manifested by incomplete self-similarity of structure strength as a function of structure size. Capturing this size effect is crucial for accurate prediction of the fracturing behavior and for measuring the cohesive fracture properties of composites.

Here, the quasi-brittle character of composites is characterized through the concept of fracture energy—the energy dissipated per unit fracture area created, and the associated tensile strength triggering postpeak softening (which together imply a finite material characteristic length). The postpeak softening behavior is described by a classical damage mechanics formulation, but at the microplane level. The same microplanes that describe the elastic behavior are used for this purpose. This involves description of the degradation of the moduli of the individual constituents (i.e., matrix and fiber) as a function of the strain vectors acting on that

microplane. The degraded moduli then yield the damaged stiffness tensor of the RUC via the same approach as described in Sec. 2. The damage evolution at material point level is formulated such that the desired strength, strain at stress peak, fracture energy, and the size effect can be predicted. In the material mesostructure, we consider mainly two mechanisms of damage—fiber damage and matrix microcracking. The unique multiscale structure of the present model makes it easy to describe these phenomena separately, as described in Sec. 3.1.

3.1 Constitutive Model of the Fibers. The fibers are the main load bearing component of the composite. So the damage to the fibers must properly be described on one microplane. As before, $E_{1'}^{\mathrm{f}}$ and $E_{2'}^{\mathrm{f}}$ denote the axial and transverse moduli of the fiber. Now let the additional superscript 0 denote the original undamaged values. For each microplane triad, we introduce two damage variables for the fiber—one denoting the axial damage $\omega_{1'}^{\mathrm{f}}$ and the other the transverse damage $\omega_{2'}^{\mathrm{f}}$. The damage variables vary from 0 in the undamaged state to 1 indicating complete failure. Thus, the following law for degradation of the fiber moduli is adopted:

$$E_{1'}^{\mathrm{f}} = (1 - \omega_{1'}^{\mathrm{f}})E_{1'}^{\mathrm{f0}}; \quad E_{2'}^{\mathrm{f}} = (1 - \omega_{2'}^{\mathrm{f}})E_{2'}^{\mathrm{f0}} \qquad (35)$$

To simulate the progressive failure behavior of composites, physically realistic damage variables evolving as a function of the microplane strain vectors must be formulated. However, unlike some other quasi-brittle materials, such as concrete and rock, formulating them is more complicated. Tests attempting to measure complete postpeak softening curve of composites struggle with extreme snapback, destabilizing the test. In view of these difficulties, this curve must be postulated intuitively and predictions checked later in structural tests. The area under this curve (dimension N/m^2) equals the fracture energy of the material (dimension N/m) divided by crack band width, which can be determined by measuring the size effect on the nominal strength of notched specimens. It is posited that the damage in tension must occur in two stages:

(1) Stage I, in which the undulating fibers straighten, along with some cracking in the matrix, and causes a sudden drop of the load; and
(2) Stage II, in which the progressive failure of the straightened fibers occurs at a gradually accelerating pace. The load drop is slow initially but accelerates toward the end as the load is shared by fewer and fewer remaining fibers.

Accordingly, the evolution of the damage variable $\omega_{1'}^{\mathrm{f}}$ is split in two parts. For the first part, corresponding to a sharp drop in the load

$$\omega_{1'}^{\mathrm{f}} = (1 + R)\left(1 - \frac{\varepsilon_N^{\mathrm{f0}}}{\varepsilon_N}\right) \quad \text{for} \quad \varepsilon_N^{\mathrm{f0}} < \varepsilon_N < \varepsilon_N^{\mathrm{f1}} \qquad (36)$$

where $\varepsilon_N^{\mathrm{f0}}$ is the strain at which the first stress drop occurs, $\varepsilon_N^{\mathrm{f1}}$ is the strain at which the progressive damage begins, and R is the material parameter controlling the slope of the initial drop. For the second part, corresponding to the progressively accelerating damage, an exponential of a power is assumed. So

$$\omega_{1'}^{\mathrm{f}} = 1 - \frac{R_1}{\varepsilon_N \exp\left(R_2 \langle \varepsilon_N - \varepsilon_N^{\mathrm{f0}} \rangle^q\right)} \quad \text{for} \quad \varepsilon_N > \varepsilon_N^{\mathrm{f1}} \qquad (37)$$

where R_1, R_2, and q are the parameters controlling the shape of the damage curve, and $\langle .. \rangle$ are the Macaulay brackets, defined as $\langle x \rangle = \max(x, 0)$. Evolution of the fiber modulus as damage progresses is illustrated in Fig. 5a for $R = 0.62$, $R_1 = 0.0082$, $R_2 = 1.6 \times 10^5$, $q = 4.25$, $\varepsilon_N^{\mathrm{f0}} = 0.00109$, and $\varepsilon_N^{\mathrm{f1}} = 0.001493$. The physical meaning of these parameters is listed in Table 3, and their calibration from tests is described in Sec. 5.3.1.

The damage variable $\omega_{1'}^{\mathrm{f}}$ is always kept to a value slightly less than unity (i.e., 0.999) to prevent potential numerical instabilities induced by zero stiffness. Under [0–90] loading, i.e., the loading along the fibers, the strength is mainly governed by parameter $\varepsilon_N^{\mathrm{f0}}$.

On the other hand, the fracture energy is governed by the parameters R, R_1, R_2, and q. As will be seen later, this form is effective in predicting correctly the size effect in structural strength.

The description of transverse damage is simpler. The effective transverse strain is defined as $\varepsilon_T = \sqrt{\varepsilon_M^2 + \varepsilon_L^2}$. Let $\varepsilon_T^{\mathrm{f0}}$ denote the strain at which the first and weakest strand of the fiber breaks under a transverse load. Then, the evolution of the transverse damage variable $\omega_{2'}^{f}$ may be described by the following equation:

$$\omega_{2'}^{\mathrm{f}} = \frac{\langle \varepsilon_T - \varepsilon_T^{\mathrm{f0}} \rangle}{\varepsilon_T^{\mathrm{fc}} - \varepsilon_T^{\mathrm{f0}}} \qquad (38)$$

Furthermore, the axial and transverse fiber damage interacts. For example, if the axial modulus degrades by $\omega_{1'}^{\mathrm{f}}$ due to axial damage, then the transverse and other moduli also degrade and vice versa. To take this interaction into account, an effective measure of fiber damage may be defined as $\omega^{\mathrm{f}} = \max(\omega_{1'}^{\mathrm{f}}, \omega_{2'}^{\mathrm{f}})$. Then, Eq. (35) becomes

$$E_{1'}^{\mathrm{f}} = (1 - \omega^{\mathrm{f}})E_{1'}^{\mathrm{f0}}; \quad E_{2'}^{\mathrm{f}} = (1 - \omega^{\mathrm{f}})E_{2'}^{\mathrm{f0}} \qquad (39)$$

Thus, all the other moduli of the fiber ($E_{3'}^{\mathrm{f}}$, $G_{1'2'}^{\mathrm{f}}$, etc.) are also assumed to be reduced in the same proportion. The Poisson ratios, as dimensionless parameters, were kept unchanged.

It has been observed that the strength of the woven composites under compression can be different than in tension (but not the modulus). Accordingly, the parameter $\varepsilon_N^{\mathrm{f0}}$ may be set to a different value for tension and compression. In the microplane approach, it is easy to distinguish between tension and compression in different directions—just by checking the sign of ε_N. For a tensorial model, this distinction can be made only in terms of the principal stresses and strains. This is another advantage of a vectorial formulation.

The damage in compression is assumed to follow a postpeak softening curve of the same shape as in tension. This is an inevitable simplification. Although the physical mechanism of damage is doubtless different under compression, typically involving the buckling of fibers followed by the formation of kink bands, no test results exist. Once they become available, the model could easily be updated.

After the damaged fiber moduli are calculated, they are used to obtain the damaged microplane stiffness tensor, followed by the damaged RUC stiffness tensor, as outlined in Sec. 2. This then yields the current damaged stress tensor from the strain tensor.

3.2 Constitutive Model of the Matrix. In woven composites under off-axis loading, diffuse microcracking in the matrix promotes a distinct nonlinear behavior before the peak load is reached. To capture it, the matrix is modeled by Mazars-type isotropic damage model, in which the damage is driven by the effective strain defined as

$$\varepsilon_{\mathrm{eff}} = \frac{2}{3}\sqrt{\varepsilon_{ij}\varepsilon_{ij}} \qquad (40)$$
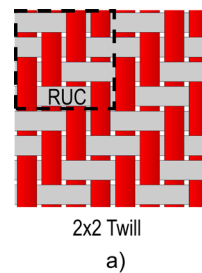
Microplane weights:

$w^\mu = 1/4$ for $\mu = 2$ and 5
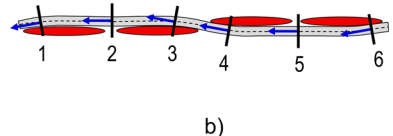
$w^\mu = 1/8$ for $\mu = 1, 3, 4$ and 6

2x2 Twill

a)

b)

Fig. 4 Schematic representation of (a) an RUC for a 2 × 2 twill weave composite and (b) the microplanes used for the discretization of the yarns

To formulate the nonlinear damage evolution law, the prepeak stress evolution under off-axis loading may be split into an initial linear part, followed by a nonlinear part. To this end, we introduce a strain cut-off ε^{m0} such that the response would be linear if $\varepsilon_{\text{eff}} < \varepsilon^{m0}$ and nonlinear otherwise. Accordingly, the stress can be written as the sum of the linear and nonlinear parts

$$\sigma = \sigma_L + \sigma_{NL} \tag{41}$$

Here, the nonlinear part of the stress is given by

$$\sigma_{NL} = E^{m0}\varepsilon^{m0} + H\langle \varepsilon_{\text{eff}} - \varepsilon^{m0} \rangle^n \tag{42}$$

where ε^{m0} is the strain at which the nonlinearity in the response begins, while H and exponent n define the curvature of the nonlinear part of response curve. Equation (41) may be rewritten as

$$\sigma_{NL} = E^{m0}\left(\frac{\varepsilon^{m0}}{\varepsilon_{\text{eff}}} + \frac{H}{E^{m0}\varepsilon_{\text{eff}}} \langle \varepsilon_{\text{eff}} - \varepsilon^{m0} \rangle^n \right)\varepsilon_{\text{eff}} \tag{43}$$

This may be expressed in the classical damage mechanics form as

$$\sigma_{NL} = E^m \varepsilon_{\text{eff}} = E^{m0}(1 - \omega^m)\varepsilon_{\text{eff}} \tag{44}$$

where E^m is the effective damaged elastic modulus of the matrix, E^{m0} is its original value, and ω^m is the damage variable for the matrix, given by

$$\omega^m = 1 - \left(\frac{\varepsilon^{m0}}{\varepsilon_{\text{eff}}} + \frac{H}{E^{m0}\varepsilon_{\text{eff}}} \langle \varepsilon_{\text{eff}} - \varepsilon^{m0} \rangle^n \right) \tag{45}$$

To describe the postpeak response, one further needs the strain at peak load, ε^{mc}, and the final strain at failure as ε^{mf}, at which the stress is reduced to zero. For lack of data, the stress after the peak load is assumed to be reduced to zero linearly, as the simplest assumption.

According to Eq. (44), the matrix Young's modulus E^m degrades as

$$E^m = (1 - \omega^m)E^{m0} \tag{46}$$

where E^{m0} is the initial undamaged value, see Fig. 5(b) for $H = 92.1$, $n = 0.5714$, $\varepsilon^{m0} = 0.007$, $\varepsilon^{mc} = 0.22$, and $\varepsilon^{mf} = 0.35$. The physical meaning of these parameters is listed in Table 3, and their calibration from tests is described in Sec. 5.3.2.

The damaged modulus is used to obtain the fourth-order stiffness tensor of the matrix plate, given by Eq. (1). Further, it is also used in the calculation of the effective properties of the yarn, which then lead to the stiffness tensor of the RUC, as outlined in Sec. 2.

The present constituent-level description of damage makes the model physically sound, conceptually clear and also easily tunable to desired experimental data. To calibrate the model for on-axis data, mainly the parameters of the fiber need to be adjusted. Likewise, the off-axis calibration is achieved by adjusting mainly the matrix parameters.

4 Experiments for Calibration and Validation of the Model

4.1 Materials. The model was calibrated and validated using data from the experiments conducted on twill 2×2 woven composite coupons. The coupons were fabricated using compression molding and consisted of an epoxy resin matrix, reinforced by carbon fibers. Each coupon, of approximate thickness 1.9 mm, consisted of eight laminae, for both layups. Two different layups, viz., the $[0]_8$ and the quasi-isotropic (QI) $[0/45/-45/90/90/-45/45/0]$, were tested in order to provide sufficient data for calibration and validation.

4.2 Uniaxial Tests. Uniaxial tests on coupons were conducted to obtain the elastic properties and strength of the composite. The following tests were conducted:

(1) The 0 deg configuration (conducted on both layups), where the loading axis is aligned with direction 1 of the RUC (see Fig. 1), to yield axial moduli and strength of the composite lamina, both under tension and compression.
(2) The 45 deg configuration (conducted for only the $[0]_8$ layup, under tension), where the loading direction is at the angle of 45 deg with direction 1 (see Fig. 1), to yield the shear modulus and strength of the lamina.

The uniaxial tension tests on the $[0]_8$ layup were used for calibration of the model, whereas those on the QI layup were used for validation. All the tests were conducted in accordance with the ASTM standards [37,38].

4.3 Size Effect Tests. Uniaxial coupon tests could not be used to measure the fracture energy because a stable postpeak is not achievable for coupon level tests on composites [24,31,36]. The tests indicate the occurrence of an extreme snapback at peak load, with a loss of stability.

The reason is that composites, while quasi-brittle, also have a very high strength and stiffness causing the stored strain energy at peak load to be very high. Accordingly, controlled energy dissipation is rather challenging.

It should be remarked that the lack of a stable postpeak in the structural response of composites has led to several failure theories based on strength. These theories can describe well the strength envelope of the composite but not the fracture behavior. Thus, they fail to predict the energetic size effect on the structural strength and postpeak energy dissipation.

This serious limitation can be overcome by performing size effect tests, which is apparently the only reliable manner to determine the fracture energy of the material, albeit indirectly (see the Appendix for more details). With the fracture energy available from size effect tests, the postpeak may be calibrated from the condition that the area under the stress–strain curve be equal to the fracture energy per unit volume of the crack band. Size effect tests were conducted on single-edge-notched tension (SENT) specimens, using the $[0]_8$ layup.

5 Calibration and Validation of the Model

5.1 Finite-Element Implementation. The present model was implemented in ABAQUS EXPLICIT v6.11 as a user material in subroutine VUMAT [39]. The structures studied were meshed using four-noded shell elements with reduced integration. For a shell element with a user-defined subroutine, the strain increment in the out-of-plane direction needs to be specified in ABAQUS. We define this increment by enforcing plane stress conditions ($\sigma_3 = 0$). For a woven composite for which $E_1 = E_2$, $\nu_{31} = \nu_{32}$, and $\nu_{21} = \nu_{12}$, this gives

$$d\varepsilon_3 = -\frac{E_1}{E_3}\frac{\nu_{31} + \nu_{21}\nu_{32}}{1 - \nu_{21}\nu_{12}}(d\varepsilon_1 + d\varepsilon_2) \tag{47}$$

Furthermore, like any material model used for strain localization and softening, a suitable localization limiter must here be introduced, to ensure objective numerical results, free from spurious mesh sensitivity [26,40–42]. Here, modeling is performed in the sense of the crack band model, in which the width of the damage localization band, w_c, is a material property. This width is also equal to the mesh size, which is here chosen as 2 mm. A change in the element size necessitates scaling of the postpeak response such that the fracture energy remain unchanged. Although changing the element size is possible (with postpeak adjustment), the crack band model is most accurate when the element size is kept equal to w_c. This size should not be confused

Table 1 Mechanical properties of the constituents

Elastic constant	Matrix	Fiber	Yarn
Axial modulus, $E_{1'}$ (GPa)	3.5 $(=E^m)$	190	134.05
Transverse modulus, $E_{2'} = E_{3'}$ (GPa)	3.5 $(=E^m)$	40	9.69
Shear modulus, $G_{1'2'} = G_{1'3'}$ (GPa)	1.7 $(=G^m)$	24	5.68
Shear modulus, $G_{2'3'}$ (GPa)	1.7 $(=G^m)$	14.3	3.57
Poisson ratio, $\nu_{1'2'} = \nu_{1'3'}$	0.35 $(=\nu^m)$	0.26	0.287
Poisson ratio, $\nu_{2'3'}$	0.35 $(=\nu^m)$	0.49	0.448

Table 2 Comparison of the measured and predicted elastic constants of the composite lamina

Elastic constant	0 deg – 90 deg configuration Measured	0 deg – 90 deg configuration Predicted	45 deg configuration Measured	45 deg configuration Predicted
$E_1 = E_2$ (GPa)	53.5	56.36	—	13.742
G_{12} (GPa)	4.49	4.649	—	27.34
$\nu_{12} = \nu_{21}$	0.04	0.031	0.84	0.724

with the size of the RUC, which is roughly 7.5 mm and merely represents the repeating geometric unit of the material.

Here, 2 mm was the best choice achieving accuracy in resolving the stress and strain fields in the structure, at a reasonable computational cost. A finer mesh of size 1 mm (with the corresponding energy-equivalent postpeak adjustment) delivered about the same results, which confirms the objectivity of the model. It did not improve the accuracy significantly but had a much higher computational cost.

5.2 Elastic Behavior. One of the salient features of the present model is its capability to *predict* the elastic properties of a composite lamina from those of the constituents, using the microplane approach. Here, predictions are made for both the above configurations. The predictions in the 0 deg configuration are governed by the elastic properties of the fiber, since they are the main loading bearing components. Likewise, in the 45 deg configuration, the predictions are governed by the properties of the matrix. The model is used to obtain the elastic properties of one RUC, as explained above. At a given material point, this is the same as the elastic properties of one lamina or one layer of the layup. Then, for a given layup, the finite-element program calculates the properties of the laminate according to the laminate theory.

To predict the elastic properties of the lamina or one RUC (i.e., K^{RUC}), the following inputs are required:

(1) Elastic properties of the matrix;
(2) Elastic properties of the fiber;
(3) Volume fractions of the fiber within the yarn, V_f^Y, and within one RUC, V_f; and
(4) Cross-sectional dimensions of the yarn (to determine the orientations of the microplane).

The properties of the constituents in the composite (i.e., items 1 and 2) were not known. So they were estimated from the literature [42]. Furthermore, according to Ref. [42], the fiber volume fraction within one yarn V_f^Y was assumed to be 0.7, and then the effective properties of the yarn were calculated according to Eqs. (17)–(21) applicable to a unidirectional composite, see Table 1. The volume fraction of the fiber within one RUC, V_f, was obtained as 0.536, according to the ASTM standard D3171-11, procedure

B [44]. Then, the volume fraction of the yarns (fill + warp) V_y within one RUC was calculated as follows:

$$V_y = \frac{\text{volume fraction of fiber within one RUC}}{\text{volume fraction of fiber within one yarn}}$$
$$= \frac{V_f}{V_f^Y} = \frac{0.536}{0.7} = 0.7661 \tag{48}$$

Thus, the volume fraction of the matrix outside the yarn was $v_m = 1 - V_y = 0.2339$.

The orientations of the microplanes were determined from the weave geometry. This was essential to account for the effect of yarn undulations on the stiffness. As described in Sec. 2, the undulation angle α, which was here 3.91 deg, determines the orientations of the microplanes. The weights of microplanes were decided upon dividing each ellipse into three parts, and then drawing the discretized undulation path. The path consisted of six segments, each corresponding to one microplane (see Fig. 4). The weight assigned to each microplane was proportional to the fraction of the yarn length occupied by that segment. So, for a twill weave, the weights were 1/8, 1/4, 1/8, 1/8, 1/4, and 1/8. Using these volume fractions, microplane orientations, weights and the properties of the yarn, the stiffness tensor of the RUC (K^{RUC}) was calculated. This yielded the elastic properties of the laminate. A schematic representation of the RUC and the microplanes considered here is shown in Fig. 4.

Table 2 shows a comparison of the measured and predicted elastic properties of the lamina under 0 deg and 45 deg configurations. Note that only the fiber modulus $E_{1'}^f$ had to be adjusted to obtain a good agreement. Other than $E_{1'}^f$, all the other elastic properties of the constituents were kept at the values obtained from the literature for similar systems. It can be seen that the agreement between the measured and predicted values is very good, for both configurations. The model is seen to predict the axial moduli of the lamina accurately. Importantly, it can also predict well the Poisson ratios and shear moduli.

This serves as a strong validation of the present model and demonstrates that it provides a significant improvement over the
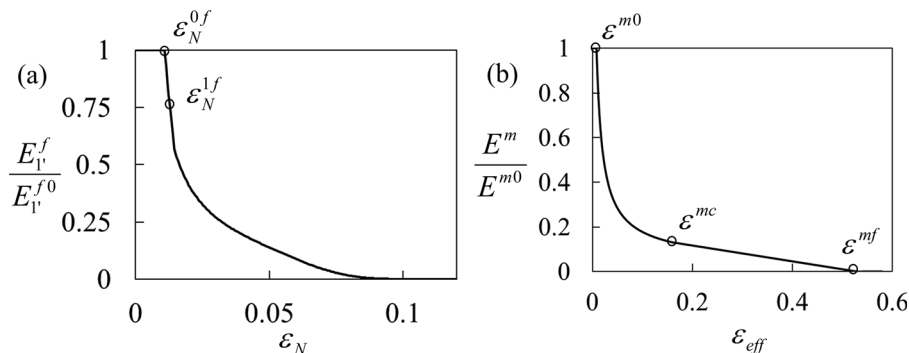
Fig. 5 Evolution laws of (a) the fiber modulus degradation and (b) the matrix modulus degradation

earlier microplane model for fiber composites. Furthermore, it should be stressed that, in contrast to various models in literature which use the measured laminate elastic properties as the input, the present model predicts the laminate properties from the constituents. The possibility to predict the orthotropic elastic constants reduces the need for repeat testing of similar composites with small differences in composition or weave type, or both. Furthermore, this also indicates that the model should be extendable to other composite architectures, such as plain weaves, satin weaves, or braided composites.

5.3 Strength and Postpeak Fracturing Behavior. Next the model must be calibrated for strength and postpeak fracturing. Similar to the elastic behavior, the strength and fracture behavior in the 0 deg configuration are governed mainly by the fiber properties, and that in the 45 deg configuration mainly by the matrix properties. Table 3 summarizes the various parameters in the model, their calibration basis and their calibrated values. Each model parameter is related to a physical property of the material. In other words, empiricism is minimized, which is an important advantage.

The calibration is performed in two steps: (1) determination of parameters from computations for one material point and (2) verification of structural response from coupon level simulations. The need to use a two-step process is explained as follows. As far as the elastic stress–strain behavior and strength are concerned, the response at one material point and of a coupon under a uniform uniaxial load must be the same. However, not so for the postpeak response. At the material point level, a stable postpeak strain softening must exist such that the area under the stress–strain curve be equal to the fracture energy per unit volume of the crack band. However, just like the experiments, a stable postpeak cannot be obtained in coupon level simulations. So, to ensure that the model dissipates the correct fracture energy, a material point calibration is required.

5.3.1 Calibration of the Fiber Constitutive Equations. For the fiber, the parameters $\varepsilon_N^{\mathrm{f0}}$, $\varepsilon_N^{\mathrm{f1}}$, R, R_1, R_2, and q are calibrated in such a way that: (1) The predicted strength match that from the $[0]_8$ coupon tests, for both tension and compression and the 0 deg configuration; (2) The area under the stress–strain curve be equal to the fracture energy divided by crack band width, based on the size effect tests (which is ≈ 75 N/mm [44,45]); and (3) The predicted size effect in strength matches the test data (as shown later). The single material point simulations were conducted with reduced integration on one shell element of size $h_e = 2$ mm. The fracture energy is given by the area under the stress versus inelastic strain curve times h_e, as shown in Fig. 6(a). The corresponding curve for compression is shown in Fig. 7(a). The calibrated parameters are presented in Table 3, and the strength values are listed in Table 4.

Following the material point calibration, a verification is performed with a coupon level simulation. For the uniaxial tensile test coupon, the dimensions were 100 mm × 40 mm × 1.9 mm, and for the compressive test they were 100 mm × 40 mm × 1.9 mm, which is in accordance with the ASTM standards [37,38]. The finite-element models for both coupons were meshed with four-noded shell elements of size 2 mm. The results for the coupon simulation are shown in Figs. 6(b) and 7(b). As expected, despite a stable postpeak at the material point level, a sudden dynamic failure of the coupon is observed at the peak load. This

Table 3 Various parameters of the model and their significance

| Parameter	Significance	Calibrated from	Config.	Calibrated value
$\varepsilon_N^{\mathrm{f0}}$	Microplane normal strain at which initial drop in load occurs (T)	Uniaxial tensile test	0 deg – 90 deg	0.0109
$\varepsilon_N^{\mathrm{f0c}}$	Microplane normal strain at which initial drop in load occurs (C)	Uniaxial compressive test	0 deg – 90 deg	0.011227
ε_N^{f1}	Microplane normal strain at which progressive softening begins	Size effect tests	0 deg – 90 deg	0.014933
R	Parameter governing the sharpness of the initial drop in stress	Size effect tests	0 deg – 90 deg	0.6216
R_1	Parameter governing the shape of the progressive fiber damage	Size effect tests	0 deg – 90 deg	0.0082
R_2	Parameter governing the shape of the progressive fiber damage	Size effect tests	0 deg – 90 deg	160,000
q	Parameter governing the shape of the progressive fiber damage	Size effect tests	0 deg – 90 deg	4.25
ε^{m0}	Effective strain at which prepeak nonlinearity begins in the matrix	Uniaxial tensile test	45 deg	0.007
ε^{mc}	Effective strain at peak load in the matrix	Uniaxial tensile test	45 deg	0.22
H	Parameter governing the shape of the nonlinear arm	Uniaxial tensile test	45 deg	92.1
n	Parameter governing the shape of the nonlinear arm	Uniaxial tensile test	45 deg	0.5714
ε^{mf}	Effective strain at complete failure in the matrix	Size effect tests	0 deg – 90 deg	0.35
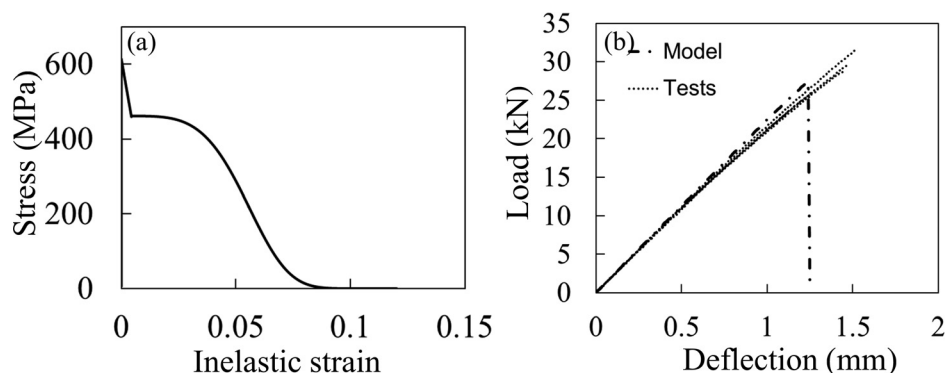
Fig. 6 (a) Degradation of fiber stress versus inelastic strain at one material point, calibrated for tension. (**b**) Comparison of the measured and predicted load displacement curve for a $[0]_8$ coupon, under tension.
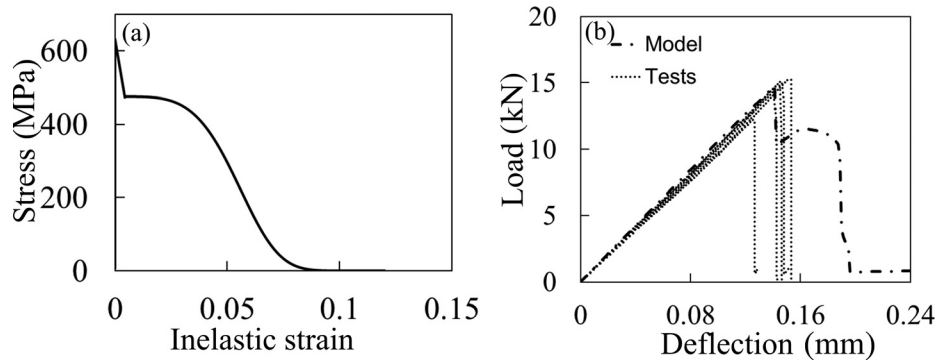
Fig. 7 (*a*) Degradation of fiber stress versus inelastic strain at one material point, calibrated for compression. (*b*) Comparison of the measured and predicted load displacement curve for a $[0]_8$ coupon, under compression.

Table 4 Comparison of the measured and predicted strengths of the $[0]_8$ laminate

Material property	Measured	Predicted
Tensile strength (MPa)	598	602.96
Compressive strength (MPa)	618	626
Shear strength (MPa)	107	108.75

can be seen as the vertical drop of load and is induced by snapback. Both figures show excellent agreement with the experiments, for both the elastic slope and the strength under tension as well as compression.

5.3.2 Calibration of the Constitutive Equations of the Matrix. The matrix parameters ε^{m0}, ε^{mc}, H, and n were calibrated at material point level, to match accurately the prepeak nonlinearity and the peak load from the $[45]_8$ coupon. The fracture energy in this configuration is not known. Thus, a conservative value of ≈ 50 N/mm was assumed, and the parameter ε^{mf} was calibrated accordingly. The material point calibration performed on one element of size 2 mm is shown in Fig. 8(*a*). The calibrated parameters are shown in Table 3, and the corresponding strength values are listed in Table 4.

Following the material point calibration, coupon level simulations were conducted for verification. The coupon dimensions, in accordance with the ASTM standards, were 100 mm × 40 mm × 1.9 mm. The coupon was meshed with a 2 mm mesh. The coupon load–deflection curves are shown in Fig. 8(*b*). It is seen that the shear response is also predicted well, including the prepeak nonlinearity caused by the constrained damage of the matrix. The strength, too, is predicted well, as can be

seen from Table 4. An instability is observed at the peak load, manifested as a vertical drop of load to zero, which is indicative of a snapback, consistent with the tests. It should be noted that the strength reported in Table 4 is calculated with respect to the initial undeformed coupon dimension. Thus, it is different from the peak value seen in Fig. 8(*a*), where the stress–strain curve shown is with respect to the current or deformed configuration.

Figure 10(*a*) compares the fracture pattern seen on this coupon with the damage localization predicted by the model. Again, note the good agreement.

It should be remarked that the prediction in the 0 deg configuration remained unaffected by the adjustment of matrix parameters. This means that the model calibration can in general follow a clear sequence, avoiding the trouble of going back and forth in loops. Thus, the conceptually clear description of the behavior of the constituents makes the calibration process straightforward.

5.4 Verification and Validation

5.4.1 Uniaxial Test on Q.I. Laminates. Following the systematic calibration, predictions are made to validate the model. The tests used for this purpose are uniaxial tests on coupons with a quasi-isotropic layup, $[0/45/-45/90/90/-45/45/0]$. The predictions are made for both tension and compression. The coupon dimensions were 100 mm × 40 mm × 1.9 mm in tension and 100 mm × 40 mm × 1.9 mm in compression, in accordance with the ASTM standards. Finite-element models of the coupons were built and meshed with shell elements of size 2 mm. The comparison of the predicted strengths can be seen in Table 5 and the load–displacement plot in Figs. 9(*a*) and 9(*b*). In both cases, the agreement in the initial slope and strength is very good.

For the tensile test, the predicted strength is slightly on the lower side. This may be attributed to the fact that the mean
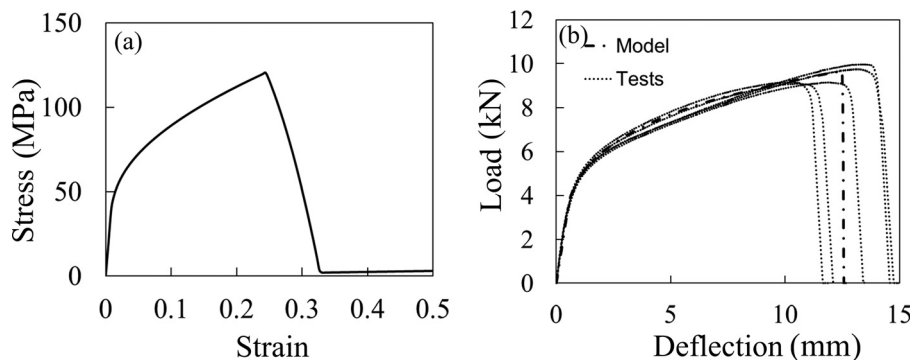

Fig. 8 (*a*) Material point stress strain curve in the $[45]_8$ configuration, under tension. (*b*) Comparison of the measured and predicted load displacement curve for a $[45]_8$ coupon, under tension.

Table 5 Comparison of the measured and predicted strength of the quasi-isotropic laminate

Material property	Measured	Predicted	% error
Tensile strength (MPa)	486	432.57	10.99
Compressive strength (MPa)	446	445.51	0.11

strength measured from the 0 deg configuration tensile test, that was used in calibration, had itself a significant scatter. The prediction of the tensile strength of the QI coupon rests heavily on this calibration. The reason is that the first layer to experience failure is indeed the layer oriented along the loading axis. This is because the strain at failure is, for this orientation, much lower. It is likely that the average tensile strength of the material is in fact higher than 598 MPa. Were this true, this prediction would be much closer to the experimental value. If more test data with a lower scatter are available, this question could be verified. Nevertheless, the agreement for the compression case is excellent, since the tests used to calibrate the compressive strength had a very low scatter. This serves as a very strong validation of the model.

It should be noted that after the first layer fails, the other off-axis layers can still bear the load. This is the reason for the load to not go to zero right away. This phenomenon may have been difficult to record in the tests, possibly due to strong dynamic effects at failure. Figures 10(b) and 10(c) show the actual fracture patterns from the tests, and the damage localization predicted by the model, which again show good agreement.

5.4.2 Size Effect Tests. The fracture energy that was indirectly measured from size effect tests was incorporated in the model by calibrating the material point response. The calibration satisfies the condition that the area under the stress–strain curve equals the fracture energy per unit volume. However, this does not guarantee that the model would be able to predict the right size effect in structural strength. This is because, for lab-scale structures of quasi-brittle materials, the FPZ might not have reached its full size when the structure reached its peak load. Therefore, the peak load is governed by not only the numerical value of the fracture energy but also by the shape of the softening law. Thus, checking the predicted size effect is an important verification of the damage formulation. Material failure theories that are based purely on strength cannot make this prediction. This aspect will be considered in detail in a subsequent article. Here, only the comparison of the predicted size effect and the available test data can be shown.

The tested SENT coupons were of three different sizes, scaled as 1:2:4. The dimensions of the smallest coupon were $L = 100$ mm, $D = 20$ mm, and $T = 1.9$ mm. The length L and width D of the medium and large specimen (though not thickness T) were scaled accordingly. Each coupon had on one edge a precut notch of length $a = 0.2D$. Finite-element models for all three
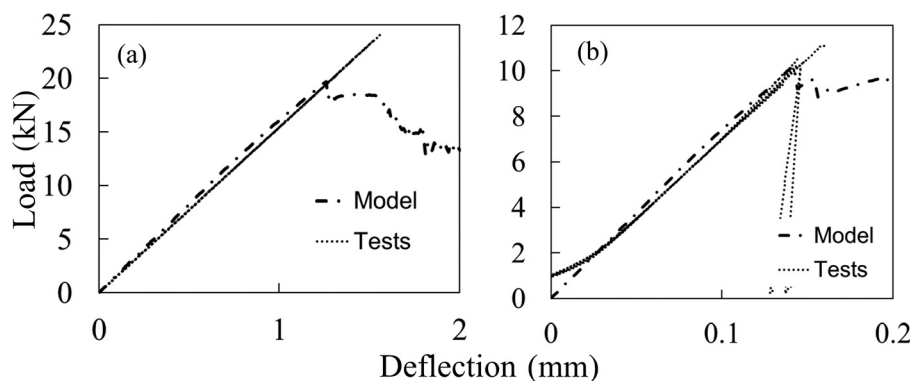

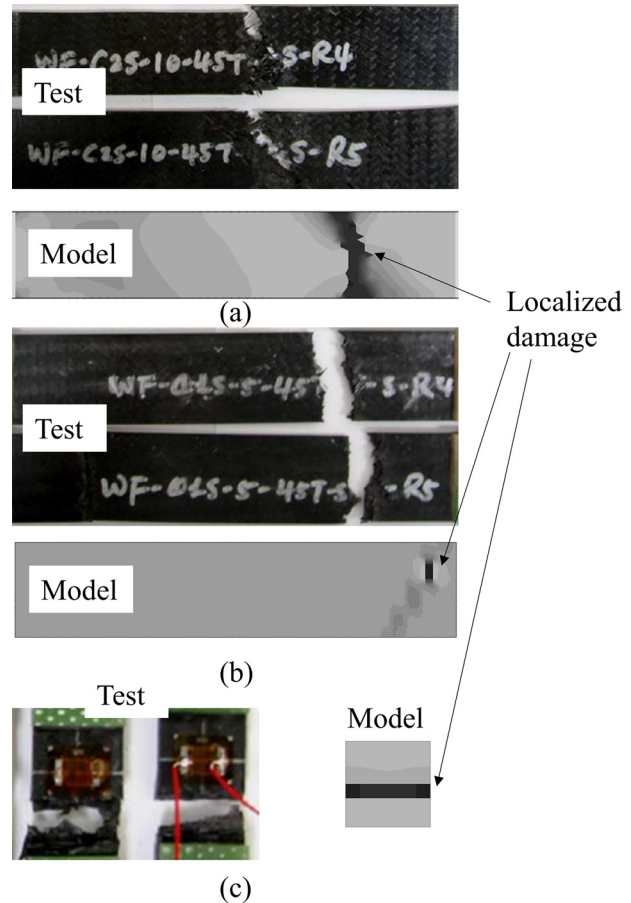**Fig. 10 Fractured specimen from the tests and predicted damage localization from simulations for (a) [45]₈ coupon under tension, (b) QI coupon under tension, and (c) QI coupon under compression**

SENT coupons were built, and uniaxial tensile simulations were performed to predict the peak load. The fracture propagation for these specimens was modeled in the sense of the crack band. The crack bandwidth h_e was 2 mm. A very fine mesh had to be used in the direction of crack growth, to capture correctly the stress profile in the ligament. Figure 11 shows a comparison of the predicted and measured strengths for the coupons of different sizes. It can be seen that, indeed, the model predicts the correct size effect. It should be noted that the specific assumed form of the fiber softening is instrumental in this prediction. Furthermore, using the size effect fitting, the fracture energy estimated from the modeling

Fig. 9 Comparison of the measured and predicted load displacement curve for a quasi-isotropic coupon under (a) tension and (b) compression
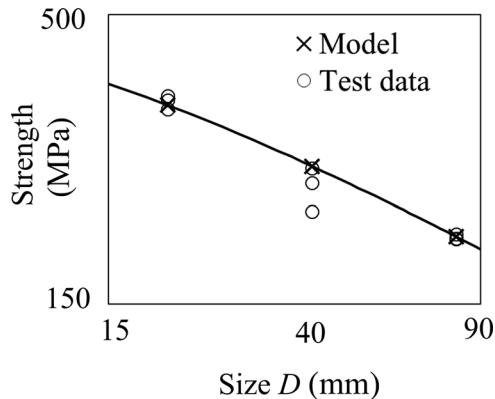
Fig. 11 Comparison of the measured and predicted size effect in SENT $[0]_8$ coupons

predictions was 80.4 N/mm, which agrees very well with the value from tests ($\approx$75 N/mm [45]). This important check provides a strong verification of the model.

6 Application to Progressive Crushing of Composite Tubes

At present, the steel structural components ensuring sufficient crashworthiness of cars are relatively heavy, increasing fuel consumption. Modern carbon composite materials have the potential to reach mechanical performance as good as, or better than, metallic materials, providing significant savings in fuel costs, and possibly in fabrication costs as well. Automobile crashworthiness is what motivated development of the present model, with the objective of modeling the front bumper crush cans, which are the main component dissipating the energy in midvelocity impacts. The metallic crush cans absorb the energy of impact by a mechanism that involves progressive plastic folding. In composites, however, the energy is dissipated through a combination of several complicated damage and fracture mechanisms including fiber breaking, matrix cracking, and possibly delamination. For accurate prediction of the energy dissipated by composites, it is essential to characterize their fracturing behavior in an objective manner.

6.1 Splaying Fracture of Hollow Composite Tubes. One commonly observed crushing mode is the splaying mode [46,47], where the crushing of a hollow composite tube is initiated by a divergent plug (initiator) of a suitable geometry. The failure mode consists of formation of continuous fronds separated by longitudinal cracks and transverse tearing. Here, we simulate this crushing mode on two different geometries (a) circular and (b) square.

The fracture of crush cans is simulated in the sense of the crack band model, with the element size of 2 mm (equal to the crack bandwidth). The diameter D of the circular crush can and the side of the square can was 68 mm. The length of both cans is 196 mm and the thickness is 1.88 mm. The layup is $[0]_8$, with each layer 0.235 mm thick. The plug initiator geometry is shown in Fig. 12(c). The geometries are meshed with four-noded planar shell elements. The bottom of the cans is fixed, and the plug has a mass of 150 kg. The impacting velocity of the plug is 35 mph. To visualize the deformation, it is a must to include element deletion in the analysis. The criterion set for element deletion was based on an effective strain. The element is removed if the effective strain measure exceeds 0.45. This is sufficiently high to ensure that full energy dissipation is accounted for from that element.

The resulting deformation modes for the circular and square crush cans are shown is Figs. 12(a) and 12(b). From the results of the analysis, it is seen that the plug initiator enables the formation of many axial intralaminar tensile cracks distributed along the
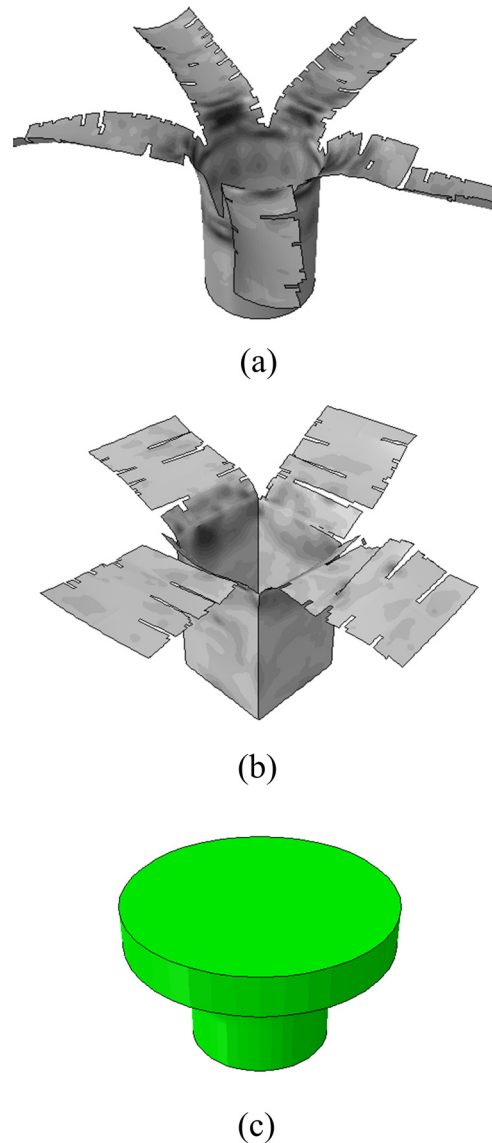

(a)

(b)

(c)

Fig. 12 Deformation patterns in (a) circular and (b) square crush cans under a plug-initiated crush and (c) geometry of the crush initiating plug

circumference, induced by tensile stresses along the hoop direction. As the crushing progresses, the plug initiator forces the material to bend outward and maintain circumferential tension throughout the entire crushing process.

To characterize the crashworthiness, the parameter measured is the plateau force. It determines the deceleration of the impacting object and governs the energy dissipated during the crash. The higher the plateau force, the higher the dissipated energy, and the better the crashworthiness. The plateau force versus the crush distance and the specific energy absorption (SEA) during the crush (the total energy absorbed by the crush can per unit mass) is computed for both geometries.

A comparison is shown in Fig. 13. It is seen that the circular can generates a much higher plateau force (21 kN) than a square can (10 kN). The SEA for the circular can is 32.78 kJ/kg while that for the square can is only 12.44 kJ/kg. The difference is explained by the deformation pattern (Fig. 12). The circular can forms five fronds, and the square can four, initiating at weak spots, the corners. More importantly, the circular can, unlike the square one, is at high circumferential tension induced by the plug, the fronds arise by localization of damage.
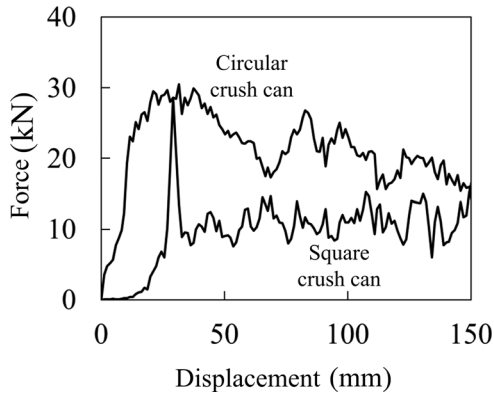
Fig. 13 Force versus displacement for (*a*) circular and (*b*) square crush can under a plug-initiated crush

As it can be seen, the circular can does not have the large initial spike in the force seen for the square can. This is largely because the plug also has a circular geometry, thereby making a smoother contact with the circular can, compared to the square can.

An interesting point to realize is that the number of fronds formed is determined by the material characteristic length represented by the crack band width. In that model, the bandwidth is a material property dictating the spacing (and thus number) of localized cracks (similarly as it dictates the initial spacing of cooling or shrinkage cracks in a halfspace). So the damage localization is central to correct predictions of the crushing force. Ignoring this fact, some previous studies in the literature induced the fronds at arbitrary spacing. This, of course, made the predictions, arbitrary, unobjective. Evidently, using the crack band model with its material characteristic length is essential.

A key advantage of using a composite material is the unique capability to tweak component performance by adjusting the layup and/or weave type. It is clear that the present model can be an effective tool to dispense with numerous costly crush tests and effortlessly evaluate a large number crush can designs with various layups, various weave architectures, various crush can constituents, various manufacturing processes, and various types of loading (e.g., by a divergent plug or by a flat plate). This is because the microplane model developed here rests on physically based approximations.

7   Conclusions

(1) The concept of microplane triads for woven composites endows the microplane model with excellent prediction capability. Based on the constituent properties and weave architecture, it provides: (a) correct predictions of all the orthotropic elastic constants and (b) realistic descriptions of the fracturing behavior.

(2) The macroscale constitutive properties can be calculated from the mesoscale model of the fibers, yarn, and polymer matrix. This multiscale feature allows clarifying the contribution of each constituent and capturing the effects of mesostructure on the elastic and fracturing behavior of woven composites.

(3) The microplane-triad model captures the highly nonlinear mechanical behavior under off-axis and shear loading, which is typical of textile composites and is characterized by diffuse subcritical microcracking of the polymer matrix.

(4) Thanks to using the crack band model, which ensures objective numerical analysis of softening damage and prevents spurious mesh sensitivity, the microplane model captures the size effect, which is a salient feature of composite structures. The size effect, too often overlooked in the composites literature, is extremely important for the safe design of large composite structures.

(5) The possibility to predict the macroscopic mechanical behavior from the constituent properties reduces the need for repeat testing of similar composites with different compositions or weave types, or both.

(6) The microplane-triad model has sufficient generality to allow extensions to composites with more complex architectures, such as the hybrid woven composites, and two- or three-dimensionally braided composites.

(7) The model realistically predicts the axial progressive crushing behavior of composite crush cans. The model is computationally efficient and capable of analyzing the fracturing behavior of large composite structures, making it a valuable design tool for crashworthiness applications.

Acknowledgment

Appendix

The size effect tests were carried out in order to measure the fracture energy of the material, G_f. Classical linear elastic fracture mechanics (LEFM) cannot be used for composites due to their inherent quasi-brittleness related to the non-negligible size of the FPZ compared to the structure size.

For an orthotropic material, the energy release rate and the stress intensity factor for an SENT specimen were solved in Ref. [48]. Their solution uses elastic parameters defined as

$$\rho = \frac{\sqrt{E_x E_y}}{2G_{xy}} - \sqrt{\nu_{xy}\nu_{yx}}, \quad \lambda = \frac{E_y}{E_x} \tag{A1}$$

where $E_x = E_y$, G_{xy}, and $\nu_{xy} = \nu_{yx}$ are the elastic constant of the woven composite. The stress intensity factor can be written as

$$K_I = \sigma\sqrt{\pi D\alpha}Y(\rho)F(\alpha) \tag{A2}$$

where σ is the nominal stress, and D is the width of the specimen. According to [48]

$$Y(\rho) = \left[1 + 0.1(\rho - 1) - 0.016(\rho - 1)^2 + 0.002(\rho - 1)^3\right]\left(\frac{1+\rho}{2}\right)^{-1/4} \tag{A3}$$

while $F(\alpha)$ is the same function of the relative crack length $\alpha = a/D$ as for isotropic materials and it depends on the geometry of the specimen and the considered boundary conditions. Now, the energy release rate for orthotropic materials can be written as

$$G(\alpha) = \sqrt{\frac{1+\rho}{2E_x E_y\sqrt{\lambda}}}K_I^2 \tag{A4}$$

Accordingly, substituting Eq. (A3) into Eq. (A4) and rearranging, one can write the energy release rate as

$$G(\alpha) = \frac{K_I^2}{E^*} = \frac{\sigma^2 D}{E^*}g(\alpha) \tag{A5}$$

where

$$E^* = \frac{1}{[Y(\rho)]^2}\sqrt{\frac{1+\rho}{2E_x E_y\sqrt{\lambda}}} \tag{A6}$$

and $g(\alpha)$ is the dimensionless energy release rate.

At fracture initiation, Eq. (A5) gives

$$G_f(\alpha) = \frac{\sigma_N^2 D}{E^*} g(\alpha) = \frac{\sigma_N^2 D}{E^*} g(\alpha_0 + c_f/D) \qquad (A7)$$

where G_f is the fracture energy, σ_N is the nominal strength of the structure, and c_f is the effective FPZ length. By expanding $g(\alpha_0 + c_f/D)$ in Taylor series and rearranging, one gets [49]

$$\sigma_N = \sqrt{\frac{E^* G_f}{D g(\alpha_0) + c_f g'(\alpha_0)}} \qquad (A8)$$

This equation relates the nominal strength of radially scaled structures to a characteristic size, D. It is used here to measure indirectly the fracture energy of the material.

An efficient way to achieve this result is by linear regression analysis of the experimental data. In fact, rearranging Eq. (A8), one can get

$$Y = AX + C \qquad (A9)$$

where $Y = 1/\sigma_N^2$, $X = D$, $A = g(\alpha_0)/E^* G_f$, and $C = c_f g'(\alpha_0)/E^* G_f$. Now, in order to get the fracture energy, one just needs to (1) perform a regression analysis, (2) get the slope, A, of the regression line, and (3) compute the fracture energy as $G_f = g(\alpha_0)/E^* A$.

References

[1] Chou, T. W., 1992, *Microstructural Design of Fibre Composites*, Cambridge University Press, New York.
[2] Bogdanovich, A. E., and Pastore, C. M., 1996, *Mechanics of Textile and Laminated Composites*, Chapman and Hall, London, UK.
[3] Bažant, Z. P., 1968, "Effect of Folding of Reinforcing Fibers on the Elastic Moduli and Strength of Composite Materials," Mekh. Polim. (Riga)/Mech. Polym., **4**, pp. 314–321 (in Russian).
[4] Ishikawa, T., and Chou, T. W., 1982, "Stiffness and Strength Behavior of Woven Fabric Composites," J. Mater. Sci., **17**(11), pp. 3211–3220.
[5] Ishikawa, T., and Chou, T. W., 1983, "One-Dimensional Micromechanical Analysis of Woven Fabric Composites," AIAA J., **21**(12), pp. 1714–1721.
[6] Naik, N. K., and Ganesh, V. K., 1992, "Prediction of On-Axes Elastic Properties of Plain Weave Fabric Composites," Compos. Sci. Technol., **45**(2), pp. 135–152.
[7] Hahn, H. T., and Pandey, R., 1994, "A Micromechanics Model for Thermoelastic Properties of Plain Weave Fabric Composites," ASME J. Eng. Mater. Technol., **116**(4), pp. 517–523.
[8] Cox, B. N., Carter, W. C., and Fleck, N. A., 1994, "A Binary Model of Textile Composites—I Formulation," Acta Metall. Mater., **42**(10), pp. 3463–3479.
[9] Scida, D., Aboura, Z., Benzeggagh, M. L., and Bocherens, E., 1998, "Prediction of the Elastic Behaviour of Hybrid and Non-Hybrid Woven Composites," Compos. Sci. Technol., **57**(12), pp. 1727–1740.
[10] Lomov, S. V., Huysmans, G., Luo, Y., Parnas, R. S., Prodromou, A., Verpoest, I., and Phelan, F. R., 2001, "Textile Composites: Modelling Strategies," Composites, Part A, **32**(10), pp. 1379–1394.
[11] Quek, S. C., Waas, A. M., Shahwan, K. W., and Agaram, V., 2003, "Analysis of 2D Triaxial Flat Braided Textile Composites," Int. J. Mech. Sci., **45**(6–7), pp. 1077–1096.
[12] Zhang, Y. C., and Harding, J., 1990, "A Numerical Micromechanics Analysis of the Mechanical Properties of a Plain Weave Composite," Comput. Struct., **36**(5), pp. 839–849.
[13] Chapalkar, P., and Kelkar, A. D., 2001, "Classical Laminate Theory Model for Twill Weave Fabric," Composites, Part A, **32**(9), pp. 1281–1289.
[14] Sankar, B. V., and Marrey, R. V., 1993, "A Unit-Cell Model of Textile Composite Beams for Predicting Stiffness Properties," Compos. Sci. Technol., **49**(1), pp. 61–69.
[15] Bažant, Z. P., and Cedolin, L., 1991, *Stability of Structures: Elastic, Inelastic, Fracture and Damage Theories*, 1st ed., Oxford University Press, New York.
[16] Naik, R. A., 1995, "Failure Analysis of Woven and Braided Fabric Reinforced Composites," J. Compos. Mater., **29**(17), pp. 2334–2363.
[17] Scida, D., Aboura, Z., Benzeggagh, M. L., and Bocherens, E., 1999, "A Micromechanics Model for 3D Elasticity and Failure of Woven-Fibre Composite Materials," Compos. Sci. Technol., **59**(4), pp. 505–517.
[18] Tsai, S. W., and Wu, E. M., 1971, "A General Theory of Strength for Anisotropic Materials," J. Compos. Mater., **5**(1), pp. 58–80.
[19] Nicoletto, G., and Riva, E., 2004, "Failure Mechanisms in Twill-Weave Laminates: FEM Predictions vs. Experiments," Composites, Part A, **35**(7–8), pp. 787–795.

[20] Huang, Z. M., 2000, "The Mechanical Properties of Composites Reinforced With Woven and Braided Fabrics," Compos. Sci. Technol., **60**(4), pp. 479–498.
[21] Carvelli, V., and Poggi, C., 2001, "A Homogenization Procedure for the Numerical Analysis of Woven Fabric Composites," Composites, Part A, **32**(10), pp. 1425–1432.
[22] Prodromou, A. G., Lomov, S. V., and Verpoest, I., 2011, "The Method of Cells and the Mechanical Properties of Textile," Compos. Struct., **93**(4), pp. 1290–1299.
[23] Lomov, S. V., Ivanov, D. S., Verpoest, I., Zako, M., Kurashiki, T., Nakai, H., and Hirosawa, S., 2007, "Meso-FE Modelling of Textile Composites: Road Map, Data Flow and Algorithms," Compos. Sci. Technol., **67**(9), pp. 1870–1891.
[24] Caner, F. C., Bažant, Z. P., Hoover, C. G., Waas, A. M., and Shahwan, K. W., 2011, "Microplane Model for Fracturing Damage of Triaxially Braided Fiber–Polymer Composites," ASME J. Appl. Mech., **133**, p. 021024.
[25] Bažant, Z. P., 1984, "Microplane Model for Strain-Controlled Inelastic Behavior," *Mechanics of Engineering Materials*, C. S. Desai and R. H. Gallagher, eds., Wiley, London, pp. 45–59.
[26] Bažant, Z. P., and Oh, B. H., 1985, "Microplane Model for Progressive Fracture of Concrete and Rock," ASCE J. Eng. Mech., **111**(4), pp. 559–582.
[27] Brocca, M., and Bažant, Z. P., 2000, "Microplane Constitutive Model and Metal Plasticity," ASME Appl. Mech. Rev., **53**(10), pp. 265–281.
[28] Bažant, Z. P., Caner, F. C., Carol, I., Adley, M. D., and Akers, S. A., 2000, "Microplane Model M4 for Concrete. I: Formulation With Work-Conjugate Deviatoric Stress," ASCE J. Eng. Mech., **126**(9), pp. 944–953.
[29] Caner, F. C., and Bažant, Z. P., 2013, "Microplane Model M7 for Plain Concrete. I: Formulation," ASCE J. Eng. Mech., **139**(12), pp. 1714–1723.
[30] Brocca, M., Bažant, Z. P., and Daniel, I. M., 2001, "Microplane Model for Stiff Foams and Finite Element Analysis of Sandwich Failure by Core Indentation," Int. J. Solids Struct., **38**(44–45), pp. 8111–8132.
[31] Cusatis, G., Beghini, A., and Bažant, Z. P., 2008, "Spectral Stiffness Microplane Model for Quasibrittle Composite Laminates—Part I: Theory," ASME J. Appl. Mech., **75**(2), p. 021009.
[32] Beghini, A., Cusatis, G., and Bažant, Z. P., 2008, "Spectral Stiffness Microplane Model for Quasibrittle Composite Laminates—Part II: Calibration and Validation," ASME J. Appl. Mech., **75**(2), p. 021010.
[33] Kirane, K., Salviato, M., and Bažant, Z. P., "Microplane Triad Model for Simple and Accurate Prediction of Orthotropic Elastic Constants of Woven Fabric Composites," J. Comput. Mater. (in press).
[34] Andrianopoulos, N. P., and Dernikas, I. T., 2013, "An Attempt to Separate Elastic Strain Energy Density of Linear Elastic Anisotropic Materials Based on Strains Considerations," Acta Mech., **224**(9), pp. 1879–1885.
[35] Daniel, I. M., and Ishai, O., 1992, *Engineering Mechanics of Composite Materials*, Oxford University Press, New York.
[36] Bažant, Z. P., Daniel, I. M., and Li, Z., 1996, "Size Effect and Fracture Characteristics of Composite Laminates," ASME J. Eng. Mater. Technol., **118**(3), pp. 317–324.
[37] ASTM, 2008, Standard Test Method for Tensile Properties of Polymer Matrix Composite Materials, ASTM International, West Conshohocken, PA, Standard No. D3039.
[38] ASTM, 2008, Standard Test Method for Compressive Properties of Polymer Matrix Composite Materials With Unsupported Gage Section by Shear Loading, ASTM International, West Conshohocken, PA, Standard No. 3410.
[39] ABAQUS, 2011, ABAQUS Users Manual, Ver. 6.11-1, Hibbitt, Karlsson and Sorensen, Pawtucket, RI.
[40] Bažant, Z. P., and Oh, B.-H., (1983). "Crack Band Theory for Fracture of Concrete," Mat. Struct., **16**(3), pp. 155–177.
[41] Jirásek, M., and Bauer, M., 2012, "Numerical Aspects of the Crack Band Approach," Comput. Struct., **110**, pp. 60–78.
[42] Blackketter, D. M., Walrath, D. E., and Hansen, A. C., 1993, "Modeling Damage in a Plain Weave Fabric Reinforced Composite Material," J. Compos. Technol. Res., **15**, pp. 136–142.
[43] Bažant, Z. P., 1976, "Instability, Ductility, and Size Effect in Strain-Softening Concrete," ASCE J. Eng. Mech. Div., **102**(EM2), pp. 331–344.
[44] ASTM, 2008, Procedure B Standard Test Methods for Constituent Content of Composite Materials, ASTM International, West Conshohocken, PA, Standard No. 3171.
[45] Salviato, M., Kirane, K., Cusatis, G., and Bažant, Z. P., "Experimental Characterization of Size Effect in Intra and Inter-Laminar Fracture in Twill Woven Fabric Composites," (in preparation).
[46] Mamalis, A. G., Robinson, M., Manolakos, D. E., Demosthenous, G. A., Ioannidis, M. B., and Carruthers, J., 1997, "Crashworthy Capability of Composite Material Structures," Comput. Struct., **37**(2), pp. 109–134.
[47] Palanivelu, S., Paepegema, W. V., Degrieck, J., Ackeren, J. V., Kakogiannis, D., Hemelrijck, D. V., Wastiels, J., and Vantommec, J., 2010, "Experimental Study on the Axial Crushing Behaviour of Pultruded Composite Tubes," Polym. Test., **29**(2), pp. 224–234.
[48] Bao, G., Ho, S., Suo, Z., and Fan, B., 1992, "The Role of Material Orthotropy in Fracture Specimens for Composites," Int. J. Solid Struct., **29**(9), pp. 1105–1116 (Corrigenda: Int. J. Solid Struct., 29, p. 2115).
[49] Bažant, Z. P., and Planas, J., 1998, *Fracture and Size Effect in Concrete and Other Quasibrittle Materials*, CRC Press, Boca Raton, FL.